PAPER • OPEN ACCESS

4D and 5D phase-space tomography using slowing-down physics regularization

View the article online for updates and enhancements.

4D and 5D phase-space tomography using slowing-down physics regularization

B.S. Schmidt[1,*], **M. Salewski**[1], **D. Moseev**[2], **M. Baquero-Ruiz**[3], **P.C. Hansen**[4], **J. Eriksson**[5], **O. Ford**[2], **G. Gorini**[6], **H. Järleblad**[1], **Ye O. Kazakov**[7], **D. Kulla**[2], **S. Lazerson**[2], **J.E. Mencke**[3], **D. Mykytchuk**[3], **M. Nocente**[6,8], **P. Poloskei**[2], **M. Rud**[1], **A. Snicker**[9], **L. Stagner**[10], **S. Äkäslompolo**[2] **and the W7-X Team**[a]

[1] Department of Physics, Technical University of Denmark, 2800 Kgs. Lyngby, Denmark
[2] Max-Planck-Institut für Plasmaphysik, Wendelsteinstr. 1, Greifswald 17491, Germany
[3] École Polytechnique Fédérale de Lausanne, Swiss Plasma Center, Lausanne, Switzerland
[4] Department of Applied Mathematics and Computer Science, Technical University of Denmark, 2800 Kgs. Lyngby, Denmark
[5] Department of Physics and Astronomy, Uppsala University, Uppsala, Sweden
[6] Dipartimento di Fisica, Università degli Studi di Milano-Bicocca, Milano, Italy
[7] Laboratory for Plasma Physics, LPP-ERM/KMS, TEC Partner, Brussels, Belgium
[8] Institute for Plasma Science and Technology, National Research Council, Milan, Italy
[9] Department of Applied Physics, Aalto University, FI-00076 Aalto, Finland
[10] General Atomics, PO Box 85608, San Diego, CA 92186-5608, United States of America

E-mail: bossc@fysik.dtu.dk

CrossMark

Abstract

We compute reconstructions of 4D and 5D fast-ion phase-space distribution functions in fusion plasmas from synthetic projections of these functions. The fast-ion phase-space distribution functions originating from neutral beam injection (NBI) at TCV and Wendelstein 7-X (W7-X) at full, half, and one-third injection energies can be distinguished and particle densities of each component inferred based on 20 synthetic spectra of projected velocities at TCV and 680 at W7-X. Further, we demonstrate that an expansion into a basis of slowing-down distribution functions is equivalent to regularization using slowing-down physics as prior information. Using this technique in a Tikhonov formulation, we infer the particle density fractions for each NBI energy for each NBI beam from synthetic measurements, resulting in six unknowns at TCV and 24 unknowns at W7-X. Additionally, we show that installing 40 LOS in each of 17 ports at W7-X, providing full beam coverage and almost full angle coverage, produces the highest quality reconstructions.

(Some figures may appear in colour only in the online journal)

---

[a] See Sunn Pedersen *et al* 2022 (https://doi.org/10.1088/1741-4326/ac2cf5) for the W7-X Team.
[*] Author to whom any correspondence should be addressed.

1. Introduction

A complete understanding of fast-ion distributions and fast-ion dynamics is imperative for future operation of fusion reactors, thus necessitating the development of ways to diagnose fast ions in both tokamaks and stellarators. Tomography is used in magnetic fusion plasma science to obtain information about fast-ion distributions, typically visualized as cross-sectional images. Assuming tokamaks to be toroidally symmetric, 3D position space (R, θ, Z) can be reduced to two dimensions (R, Z). Similarly, the fast gyration of the ions leads to azimuthal symmetry in 3D velocity space, since the gyroangle γ becomes ignorable, so the velocity space reduces to $(v_\parallel, v_\perp)$ [1]. Here, $v_\parallel$ is the magnitude of the velocity component parallel to the magnetic field and $v_\perp$ the magnitude of the velocity component perpendicular to the magnetic field. Hence, the 6D phase space consisting of 3D position space and 3D velocity space is usually reduced to a 4D phase space, as can be done in the TRANSP or ASCOT codes [2–5]. Since stellarators do not possess toroidal symmetry in position space, the phase space in stellarator plasmas can only be reduced to 5D, as in the BEAMS3D code [6, 7]. Here, we consider 4D and 5D phase-space distributions at TCV and Wendelstein 7-X (W7-X) as examples for tokamaks and stellarators.

Position-space tomography provides spatial information about fast-ion distributions. For example, the spatial location of neutron emission has been reconstructed using the 19 available neutron cameras at JET [8–11]. During the last decade, fast-ion velocity-space tomography was developed, which provides insight into the fast-ion velocity-space distribution functions from experimental data. This technique has been applied to several diagnostics, including fast-ion D-alpha (FIDA) spectroscopy [12–20], collective Thomson scattering (CTS) [21], neutron emission spectrometry [22, 23], γ-ray spectrometry [22, 23], and scintillator-based fast-ion loss detectors (FILDs) [24, 25] at the tokamaks ASDEX Upgrade, JET, EAST, MAST, and DIII-D. Velocity-space tomography has also been used to estimate 1D velocity distribution functions [26, 27]. While the 1D and 2D techniques infer velocity distribution functions in a small volume in the plasma, orbit tomography infers a 3D phase-space distribution of all fast ions in the plasma [28]. This technique uses fast-ion orbits as prior information and exploits that velocity distribution functions can, assuming toroidally symmetric plasmas, be parameterized in terms of fast-ion drift orbits by three parameters: the energy, the magnetic moment, and the canonical toroidal angular momentum. In this paper, we develop techniques to infer 4D and 5D phase-space distribution functions based on slowing-down physics regularization. The idea is to use the known physics of the slowing-down process of fast ions in plasmas as a prior in the ill-posed inference problem. This allows for reconstruction of the velocity space distribution function for all spatial locations and not just a single diagnostic locations as has been the case for previous tomographic and reconstruction techniques. This approach was demonstrated for 2D velocity-space tomography [17], which we here extend up to 5D.

Reconstructing 4D and 5D phase-space distribution functions in magnetically confined plasmas has never been attempted. A standard 4D or 5D inference appears out of reach due to the large number of unknowns, for example, discretizing each dimension by 30 points yields on the order of 10^6 grid points in 4D and 10^7 in 5D. Standard regularization techniques, such as Tikhonov regularization without additional prior information, can work in 1D, 2D, or 3D, but additional prior information is needed at present to enable the inference of the larger number of parameters in the 4D or 5D phase-space distributions. Here, we develop slowing-down physics regularization in 4D and 5D based on projected velocity spectra to show that this technique can obtain the 4D and 5D fast-ion phase-space distribution functions for plasmas heated by neutral beam injection (NBI) at TCV and W7-X. Slowing-down physics regularization also works for other plasma heating schemes such as electromagnetic wave heating in the ion cyclotron range of frequencies (ICRF). The slowing down of energetic ions by collisions always occurs in plasmas, irrespective of any other processes occurring in addition to the slowing down. Thus, this project investigates neoclassical slowing-down with the possibility of extending to non-neoclassical regimes.

In section 2, we describe the beam configurations at TCV and W7-X. In sections 3 and 4, we describe the forward problem and the Tikhonov regularization approach typically used for velocity-space tomography. In section 5, we develop the slowing-down physics regularization technique. In section 6, we describe the synthetic dataset used for our investigations. In section 7, we show and interpret the results from applying slowing-down physics regularization to synthetic data from TCV and W7-X. In section 8, we present a conclusion and outlook.

2. NBI configurations at TCV and W7-X

NBIs inject energetic particles, typically hydrogen isotopes, which have been accelerated to energies in the 10–100 keV range. In the acceleration stage, in addition to the neutral deuterium atoms, deuterium dimers and trimers are formed. As all three species are accelerated in the same potential, the energy of the injected dimers and trimers is the same as for the deuterium monomers. Hence, the velocity is reduced by a factor of $1/\sqrt{2}$ for the dimers and $1/\sqrt{3}$ for the trimers. The dimers and trimers are ionized as they exit the NBI beam and enter the plasma. Thus, when the dimers and trimers split into single deuterium ions inside the plasma due to collisions, the resulting deuterium monomers continue moving at lower velocities.

TCV has two NBIs positioned as shown in figure 1(*a*) for a top view of TCV. The NBIs are oriented tangentially to the magnetic axis in the midplane ($Z = 0$). The diagnostic FIDA lines of sight considered in this study are those used for shot 68 407 consisting of 10 horizontal and 10 vertical FIDA views. A crucial parameter for the velocity-space sensitivity of diagnostics is the viewing angle ϕ between the line of sight and the magnetic field. The viewing angle intervals for the

(a)

(b)
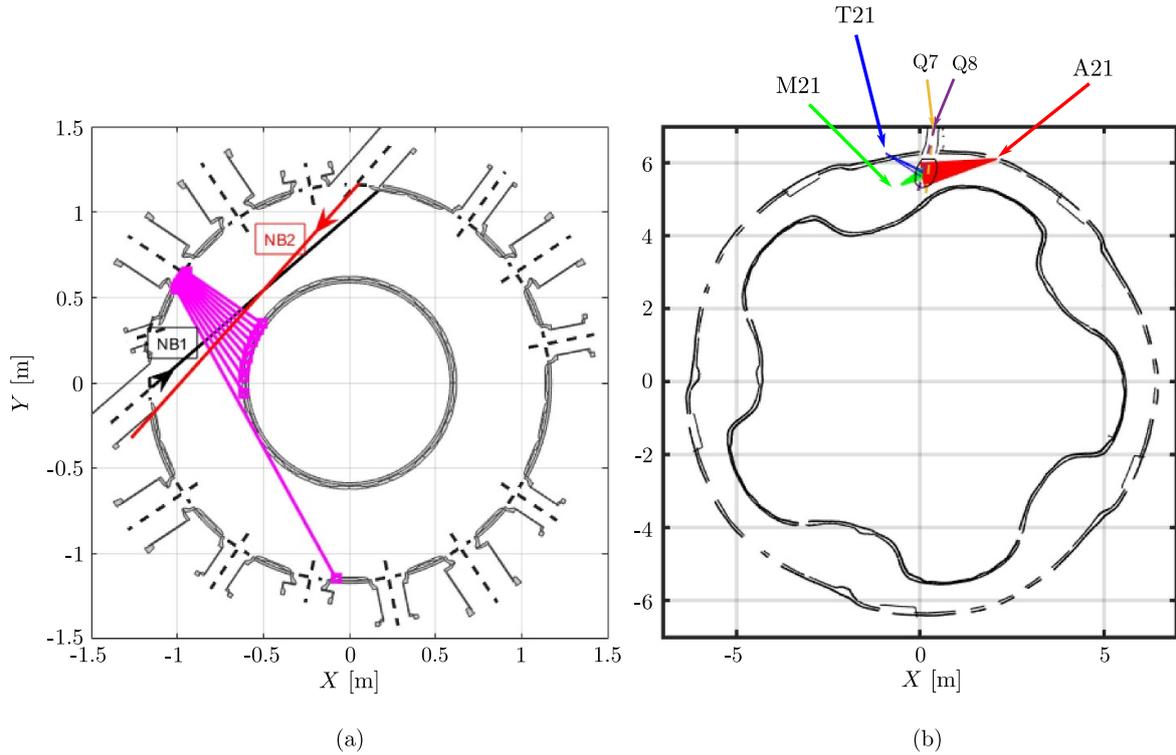
Figure 1. Neutral beam (NB) locations at (*a*) TCV and (*b*) W7-X. For TCV, the black and red lines indicate NB1 and NB2. The magenta lines indicate the lines of sight of the FIDA views. For W7-X, Q7 and Q8 correspond to the 7th and 8th NBs out of eight in total. The three fans 'A21', 'M21', and 'T21' indicate FIDA lines of sight located in the first half-module of the second module.

(a)　　　　　　　　(b)
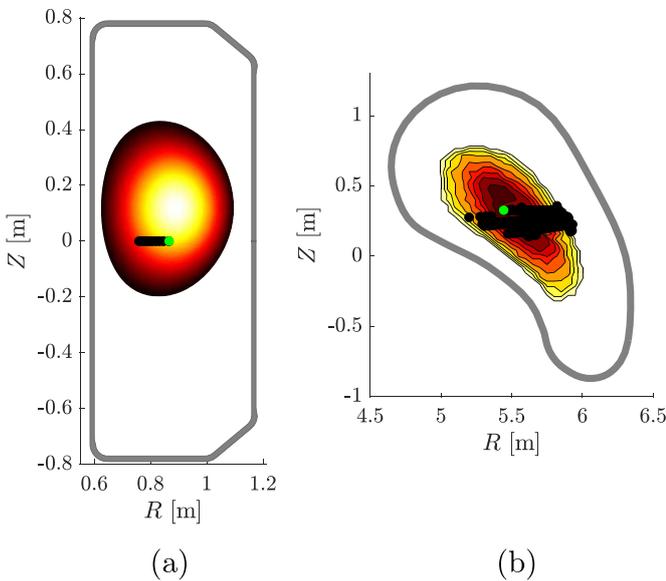
Figure 2. Poloidal cross sections and simulated fast-ion density distributions in (*a*) TCV and (*b*) W7-X at $\theta \approx 90°$. The black dots indicate the measurement volumes. The green dots indicate the locations for the distributions in figures 4 and 5.

horizontal and vertical fans are $\phi_{\text{hor}} \in [45°, 90°]$ and $\phi_{\text{vert}} \in [75°, 90°]$. The intersections of the NBIs and the FIDA lines of sight are illustrated in figure 1(*a*) as the points where the magenta lines meet the black and red lines and in figure 2 as the black dots. The nominal power fractions of the injected deuterium species at full, half, and one-third injection energy for NB1 and NB2 at TCV are 0.73:0.22:0.05 and 0.59:0.33:0.08 at the nominal energies 25 keV and 47 keV.

W7-X is designed with two NBI boxes with four beams in each [29, 30]. The two NBI boxes are positioned to achieve different injection angles for the eight beams with the local toroidal magnetic field. Beams 2, 3, 6, and 7 are pointed more radially and beams 1, 4, 5, and 8 more tangentially. The diagnostic FIDA lines of sight intersect beams 7 and 8 (Q7 and Q8); see figure 1(*b*) for an illustration of the experimental setup. Each FIDA view is part of one of three fans, originating from ports AEA21, AEM21, and AET21. We will refer to them as fans A21, M21, and T21 with corresponding viewing angle intervals $\phi_{\text{A21}} \in [2°, 10°], \phi_{\text{M21}} \in [125°, 135°]$, and $\phi_{\text{T21}} \in [35°, 45°]$. In addition to these three fans, we investigate how much information can be gained by installing additional FIDA views. Seventeen ports located in the first- and second half-modules of the second module are available for installing diagnostic FIDA views on Q7 and Q8. Figure 2 shows the spatial fast-ion distribution at TCV and W7-X along with the measurement volumes. The possible viewing angles for each port along NBI Q7 and Q8 are illustrated in figure 3. For a given port, the median viewing angle is displayed as a circle and maximum and minimum viewing angles are indicated by the top and bottom bars. Observe that with the 17 ports combined, coverage of all viewing angles is attained except for the viewing angles between approximately 10° and 20°.
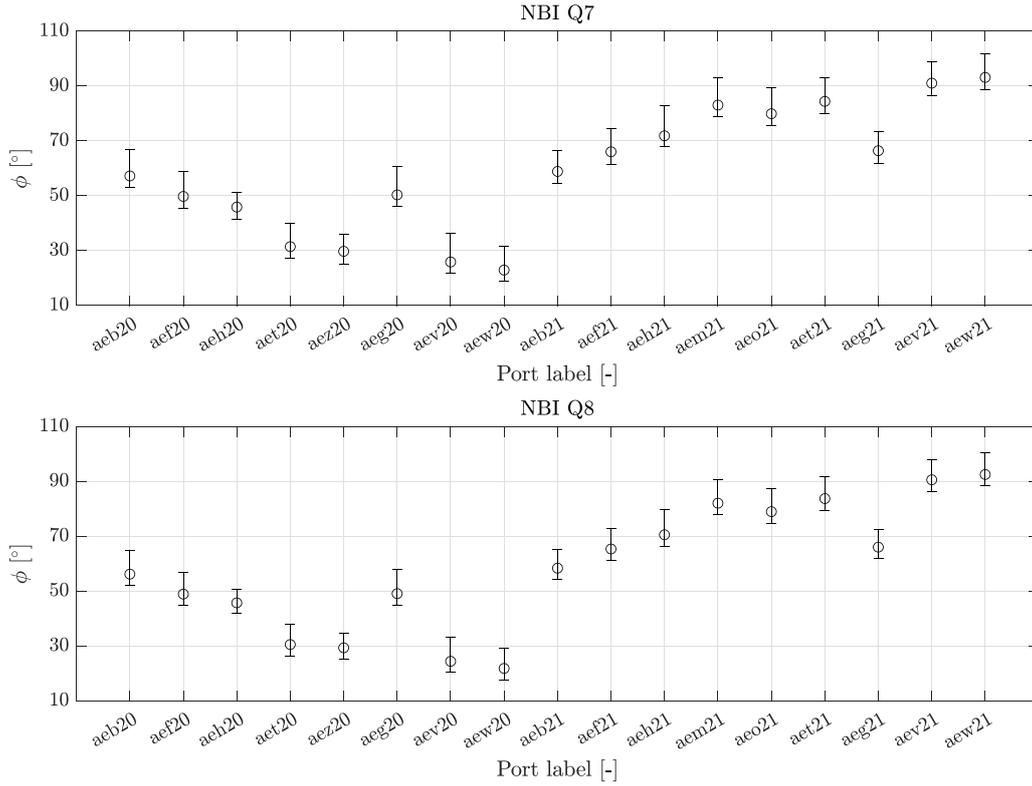
Figure 3. 17 diagnostic ports could be used for FIDA views at W7-X. The upper figure shows the viewing angles ϕ of the lines of sight and the magnetic field for NBI Q7, and the lower for NBI Q8. The circles represent the median viewing angle, and the vertical bar represents the angle range.

The power fractions of the injected deuterium species at full, half, and one-third injection energy at W7-X are 0.45:0.45:0.10 with full injection energy of 55 keV.

3. Forward model

The goal in this study is to obtain the 4D and 5D fast-ion phase-space distribution function from projections of the velocity distribution function. Such projections serve as a proxy for CTS and FIDA spectra, since the projected velocity is proportional to the Doppler shift, which is the key effect leading to the spectrum formation. However, other details such as Stark splitting are neglected.

The projections s are obtained as the integral over phase-space of the product wf, where $w = w(\lambda_1, \lambda_2, \phi, \boldsymbol{x}, \boldsymbol{v})$ is the weight function and $f = f(\boldsymbol{x}, \boldsymbol{v})$ is the phase-space distribution function [31–34]. Hence,

$$s(\lambda_1, \lambda_2, \phi) = \int_{\boldsymbol{v}} \int_{\boldsymbol{x}} w(\lambda_1, \lambda_2, \phi, \boldsymbol{x}, \boldsymbol{v}) f(\boldsymbol{x}, \boldsymbol{v}) \, \mathrm{d}\boldsymbol{x} \mathrm{d}\boldsymbol{v} \quad (1)$$

for a detected signal $s(\lambda_1, \lambda_2, \phi)$ in the wavelength bin $\lambda_1 < \lambda < \lambda_2$ with projection angle ϕ originating from a small measurement volume. A weight function, the kernel in equation (1), indicates the sensitivity of the given diagnostic at a specific location in phase-space for a projection angle ϕ and a wavelength bin with lower wavelength λ_1 and upper

wavelength λ_2. Such weight functions have also been calculated for neutron emission spectroscopy [35–38], gamma-ray spectroscopy [39, 40], FILDs [41], ion cyclotron emission [27], and MeV-proton diagnostics [42].

Discretizing position and velocity space transforms the equation into the matrix-vector equation

$$\boldsymbol{Wf} = \boldsymbol{s}, \quad (2)$$

where $\boldsymbol{f}$ is the vector corresponding to the fast-ion phase-space distribution function and $\boldsymbol{s}$ the measurement data vector corresponding to the projections. The problem formulation assumes the underlying problem to be linear. Equation (2) for 4D and 5D phase space distributions is the same as the 2D velocity-space tomography [43, 44] and 3D orbit tomography [28] formulations. The fast-ion distribution vector $\boldsymbol{f}$ has dimension n, the measurement data vector $\boldsymbol{s}$ has dimension m and contains all spectral data from all lines of sight, and $\boldsymbol{W}$ has dimension $m \times n$. The fast-ion distribution function is obtained by solving the inverse problem given by equation (2), i.e. computing $\boldsymbol{f}$ given $\boldsymbol{s}$ and $\boldsymbol{W}$.

4. Tikhonov regularization

The accuracy of the solution to the matrix equation $\boldsymbol{Wf} = \boldsymbol{s}$ is bounded by its condition number $\kappa(\boldsymbol{W}) = \sigma_1/\sigma_n$ defined as the ratio of the largest singular value σ_1 to the lowest singular

value σ_n. The condition number expresses the maximum ratio of the relative error in $\boldsymbol{f}$ to the relative error in $\boldsymbol{s}$. Therefore, a large condition number implies that a small change in $\boldsymbol{s}$ can cause a large change in $\boldsymbol{f}$. For both TCV and W7-X, $\kappa(\boldsymbol{W}) \gg 10^{15}$, so even little noise in $\boldsymbol{s}$ can cause large changes in $\boldsymbol{f}$. Such large condition numbers result from the underlying continuous problems, described, e.g. by equation (1), being notoriously ill-posed inverse problems. Condition numbers on the order of 10^{15} are typical for such ill-posed problems. Well-conditioned problems typically have $\kappa(W) \lesssim 10^4$.

Meaningful solutions to such problems can be found by regularization, which penalizes undesired features in $\boldsymbol{f}$ so that small changes in $\boldsymbol{s}$ lead to small changes in $\boldsymbol{f}$. This can be achieved by regularizing on $\boldsymbol{f}$ with a matrix $\boldsymbol{L}$ such that $\|\boldsymbol{Ls}\|_2$ is a prior for the sought solution, e.g. smoothness by choosing $\boldsymbol{L}$ to be a gradient operator. With this approach, the inverse problem can be written as the following minimization problem:

$$\boldsymbol{f}^* = \underset{\boldsymbol{f}}{\mathrm{argmin}} \, \|\boldsymbol{Wf} - \boldsymbol{s}\|_2^2 + \lambda^2 \|\boldsymbol{Lf}\|_2^2. \tag{3}$$

The value of the regularization parameter λ controls how well the solution fits the noisy data and the degree to which the regularization influences the solution. To illustrate how equation (2) is solved in practice, equation (3) can be written as

$$\boldsymbol{f}^* = \underset{\boldsymbol{f}}{\mathrm{argmin}} \left\| \begin{pmatrix} \boldsymbol{W} \\ \lambda\boldsymbol{L} \end{pmatrix} \boldsymbol{f} - \begin{pmatrix} \boldsymbol{s} \\ 0 \end{pmatrix} \right\|_2^2. \tag{4}$$

This is the most stable formulation of the inverse problem and the best suited for numerical computations [14].

Typically, it is helpful to use additional prior information to find a better solution. Previous work in velocity-space tomography in fusion plasmas has implemented non-negativity of the fast-ion distribution function, penalty matrices with different properties, null-measurement regions, specification of NBI locations, and numerical simulations as prior information. See, e.g. [14, 16–18, 45] for applications of different prior information. Here, we implement prior information by constraining the solution to lie in the vector space spanned by the expected 4D or 5D slowing-down distribution functions of fast ions assuming neoclassical transport.

5. Slowing-down physics regularization

We reconstruct simulated fast-ion phase-space distribution functions from NBI at TCV and W7-X. The ions are born by ionization of neutrals from the neutral beams at full, half, and one-third injection energies. The fast-ion distribution in velocity space is anisotropic due to the narrow pitch range of injected particles determined by the geometry of the NBI relative to the magnetic field. The fast ions are assumed to follow neoclassical slowing down due to collisions with electrons and ions in a thermal background plasma. In 2D velocity space assuming a spatially homogeneous plasma, velocity distributions arising in these situations can be modeled as anisotropic

slowing-down velocity distributions [1]. Here, we use ASCOT [5] and BEAMS3D [6, 7] to calculate 4D and 5D phase-space distribution functions assuming only the neoclassical slowing-down physics. In the remainder of this paper, we will simply call them 'slowing-down distributions'.

Thus, we postulate that the solution to equation (4) must be closely related to the anisotropic slowing-down distributions from the NBI sources at full, half, and one-third injection energies. Madsen *et al* followed a similar approach for computing 2D fast-ion velocity distribution functions resulting from co- and counter-current NBIs at EAST with good results [17].

We denote the N_{sd} phase-space slowing-down distribution functions by $\psi_1, \psi_2, \ldots, \psi_{N_{\mathrm{sd}}}$ defined for the 4D and 5D phase spaces at TCV and W7-X, where N_{sd} is the desired number of vectors in the slowing-down physics basis. In slowing-down physics regularization, the phase-space distribution function is assumed to lie in the space spanned by the set $\{\psi_j\}, j = 1, 2, \ldots, N_{\mathrm{sd}}$, so

$$\boldsymbol{f} = \sum_{j=1}^{N_{\mathrm{sd}}} c_j \psi_j, \tag{5}$$

where $c_j \in \mathbb{R}$ is the coefficient corresponding to the *j*th slowing-down distribution. Thus, we enforce slowing-down physics on the regularized solution. The energy components of the neutral beams at TCV are illustrated in figure 4. The full energy component of all eight beams at W7-X is illustrated in figure 5. Observe the sign difference of the peaks in $v_\parallel$ indicating the difference in injection direction with respect to the local magnetic field. The spatial locations for the velocity distributions are from the central locations marked by green dots in figure 2.

To enable the detection of anomalous phenomena based on experimental data, future work will use thousands of slowing-down distribution functions. The greater flexibility of the model should allow modeling anomalous transport. A single neutral beam injects fast ions with three different energies. Thus, for TCV, two neutral beams result in $2 \times 3 = 6$ distinct slowing-down basis functions ψ_j. For W7-X, eight neutral beams result in $8 \times 3 = 24$ distinct slowing-down basis functions.

Let $\boldsymbol{\Psi}$ be a matrix containing sampled values of the slowing-down distribution functions as column vectors, and let $\boldsymbol{c}$ be a column vector containing the coefficients c_j corresponding to each ψ_j. Then

$$\boldsymbol{f} = \boldsymbol{\Psi}\boldsymbol{c}, \tag{6}$$

so

$$\boldsymbol{s} = \boldsymbol{Wf} = \boldsymbol{W}(\boldsymbol{\Psi}\boldsymbol{c}) = (\boldsymbol{W}\boldsymbol{\Psi})\boldsymbol{c}. \tag{7}$$

According to equation (7), we can calculate a synthetic measurement, given the coefficients $\boldsymbol{c}$, using the weight function matrix as always used in velocity-space tomography and the matrix containing the slowing-down distribution basis functions as columns. Thus, to solve the original inverse problem
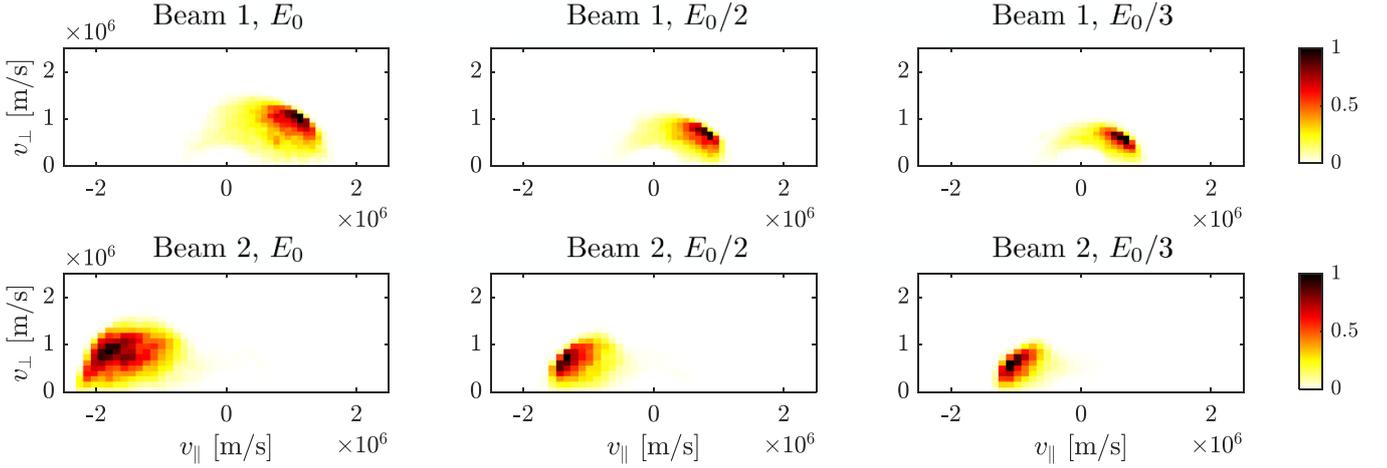
Figure 4. 2D velocity distribution functions for the full, half, and one-third energy for NB1 (top row) and NB2 (bottom row) at TCV. The distributions originate from the green dot in figure 2(*a*).
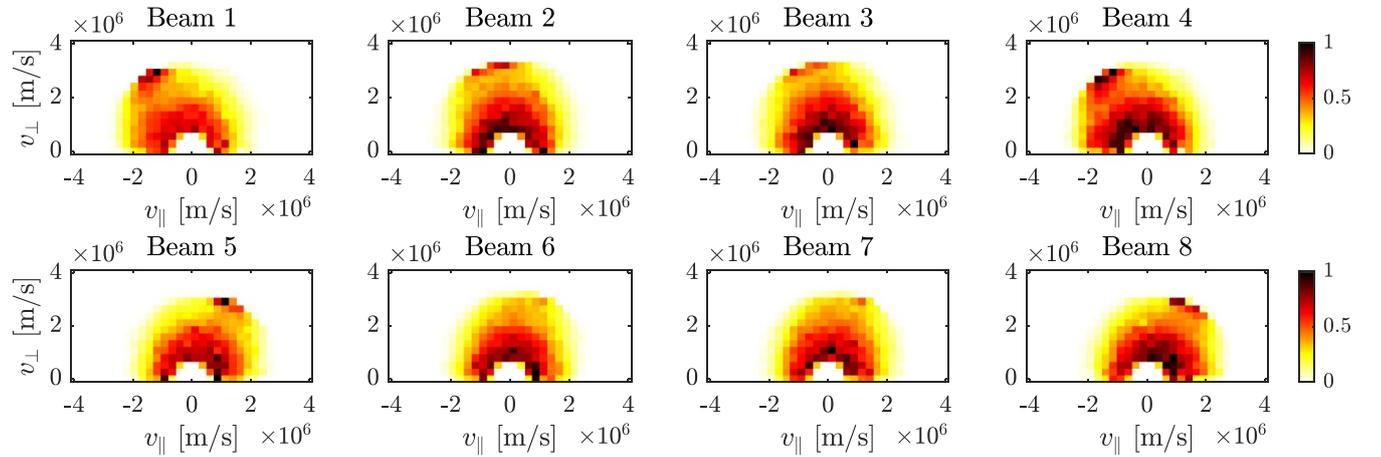
Figure 5. 2D velocity distribution functions for the full energy neutral beam injections at W7-X. The distributions originate from the green dot in figure 2(*b*).

in equation (3), we need to determine the 6 and 24 slowing-down distribution function coefficients for TCV and W7-X. Thus, our problem is to infer the densities of the NBI sources at full, half, and one-third energies from projections in velocity space at the position-space locations of the measurement volumes. These coefficients are found by solving the inverse problem in equation (7), which is to determine the coefficient vector c given s and the matrix $W\Psi$. This inverse problem will be solved by regularizing the coefficient vector c for solutions $f \in \mathrm{span}\{\psi_j\}$ using Tikhonov regularization. The underlying complexity of the modeled systems with dimensionality of 4D or 5D for TCV and W7-X therefore does not affect the solution.

5.1. Interpretation of the expansion in slowing-down functions as slowing-down physics regularization

The traditional formulation of the problem with Tikhonov regularization, with a non-negativity constraint on the solution, is

$$f^* = \arg\min_f \left\{ \|Wf - s\|_2^2 + \lambda^2 \|Lf\|_2^2 \right\} \quad \text{subject to} \quad f \geqslant 0. \tag{8}$$

Here, the matrix L determines the type of regularization that is applied; L can be the identity matrix or a discrete approximation to a derivative operator. For details on this approach, see [46], and for its use in velocity-space tomography see, e.g. [14].

We can expand the solution in terms of this basis and write $f = \Psi c$. Here, $\Psi \in \mathbb{R}^{n \times N_{sd}}$ is the matrix whose N_{sd} columns are the discretized slowing-down functions, and $c \in \mathbb{R}^{N_{sd}}$ is a vector of the coefficients in this basis. Thus, the problem in equation (8) can be reformulated as

$$c^* = \arg\min_c \left\{ \|W\Psi c - s\|_2^2 + \lambda^2 \|L\Psi c\|_2^2 \right\} \quad \text{subject to} \quad \Psi c \geqslant 0. \tag{9}$$

In this formulation, $W\Psi$ is the matrix connecting the coefficient vector c to the measurements, and $L\Psi$ is the

6

regularization matrix. The two formulations (8) and (9) are equivalent when we set $f = \Psi c$.

In this work, we take a different approach that utilizes the physics-informed basis vectors in Ψ as a prior. Specifically, instead of enforcing regularization directly on f we regularize the coefficient vector c via a regularization term $\|c\|_2^2$. This is needed since the problem $\min \|W\Psi c - s\|_2^2$ is ill-posed. Enforcing this regularization ensures that all the expansion coefficients are bounded and that the solution expressed in the slowing-down basis is physically meaningful for the given measurement scenario. The physics-informed Tikhonov regularization problem then takes the form

$$c^* = \arg\min_c \left\{ \|W\Psi c - s\|_2^2 + \lambda_c^2 \|c\|_2^2 \right\} \quad \text{subject to} \quad \Psi c \geqslant 0,$$
(10)

from which we determine the regularized 4D or 5D fast-ion phase-space distribution function f^* from

$$f^* = \Psi c^*.$$
(11)

The number of rows of the matrix $W\Psi$ is determined by the number of lines of sight and the spectral resolution. For $N = 250$ lines of sight, each with a spectral resolution of 84 measurement bins in a spectrum, $W\Psi$ has 21 000 rows. Since the matrix Ψ with the slowing-down basis consists of six simulated fast-ion phase-space slowing-down distribution functions for TCV, and 24 simulated fast-ion phase-space slowing-down distribution functions for W7-X, the matrix $W\Psi$ has six columns for TCV and 24 columns for W7-X. The interpretation of the regularization procedure by imposing the slowing-down basis prior depends on the dimension of the slowing-down basis N_{sd} compared to the number of rows n of Ψ, i.e. how many grid points the slowing-down function is resolved in.

Consider the simplest case $N_{sd} = n$. This case appears when every grid point in the discretization of phase-space is considered as a source for a slowing-down basis function. This is the approach previously demonstrated in the 2D velocity-space tomography problem [17]. If $N_{sd} = n$, the matrix Ψ is square, and numerical testing shows it has full rank. Then $f = \Psi c \Leftrightarrow c = \Psi^{-1} f$, and therefore equations (10) and (11) are equivalent to the problem

$$f^* = \arg\min_f \|Wf - s\|_2^2 + \lambda_c^2 \|\Psi^{-1} f\|_2^2 \quad \text{subject to} \quad f \geqslant 0.$$
(12)

A comparison of equations (3) and (12) shows that the expansion in slowing-down basis functions can be interpreted as a regularizer $L = \Psi^{-1}$ in the regularization term in equation (3). We shall now demonstrate that the same interpretation holds when $N_{sd} \neq n$.

We first consider the case $N_{sd} > n$ where we use more slowing-down basis functions than the number of grid points (an overcomplete system) we have chosen to discretize the distribution function. In this case, numerical testing shows that the matrix Ψ has full row rank, i.e. the $n \times N_{sd}$ matrix has rank n. We still assume that $f = \Psi c$. Then it follows from the theory in [46, section 8.4, case 2] that the matrix L in (9) must satisfy $L^\dagger = \Psi$, where the superscript $\dagger$ denotes the pseudoinverse. This, in turn, implies that $L = \Psi^\dagger$. Thus, regularizing on the coefficient vector c can be interpreted as using the regularizer $\Psi^\dagger$ for f in the regularization term in the original problem formulation.

Next, consider the case $N_{sd} < n$ where we use fewer slowing-down basis functions, and hence fewer coefficients, than the number of grid points. In this case, numerical testing shows Ψ has full column rank, i.e. the $n \times N_{sd}$ matrix has rank N_{sd}. To analyze this case, we cannot use the theory in [46] and instead we introduce the QR factorization

$$\Psi = (Q, Q_0) \begin{pmatrix} R \\ 0 \end{pmatrix} = QR,$$
(13)

where R is an upper triangular matrix, Q and Q_0 have orthonormal columns, $Q^T Q_0 = 0$, and $\text{range}(Q_0) = \text{range}(\Psi)^\perp = \text{null}(\Psi^T)$. Let $\mathcal{P} = Q_0 Q_0^T$ be the orthogonal projector on $\text{null}(\Psi^T)$. For a general f and some vector w of appropriate dimension, $f = \Psi c + Q_0 w$, so

$$\Psi c = QRc = f - Q_0 w \quad \Leftrightarrow \quad c = R^{-1} Q^T f = \Psi^\dagger f.$$
(14)

We want $f \in \text{range}(\Psi)$, so $Q_0 w = \mathcal{P}f = 0$. Thus, the problem formulation becomes

$$f^* = \arg\min_f \|Wf - s\|_2^2 + \lambda^2 \|\Psi^\dagger f\|_2^2 \quad \text{subject to} \quad \mathcal{P}f = 0.$$
(15)

Again, regularization on the coefficient vector c can be interpreted as a regularizer $L = \Psi^\dagger$ for f in the regularization term in the original problem formulation with the additional requirement that $\mathcal{P}f = 0$. This requirement corresponds to finding solutions in the vector space ψ_j described by slowing-down physics. The requirement is automatically satisfied when we compute $f = \Psi c = QRc$.

We have thus shown that we can interpret the regularization on the coefficient vector c as regularization on f in terms of slowing-down physics for any combination of n and N_{sd}. In reconstruction problems without using basis functions, we choose the number of grid points n based on the number of available measurements. Specifically, n should be similar to the number of measurements m. (It does not have to be the exact same number of unknowns as equations since the regularization provides additional requirements on the solution.) Following the same reasoning, we can choose the number of slowing-down basis functions to be similar to the number of measurements (where the data points of a measured spectrum are counted individually). The preceding analysis shows that we can choose the number of grid points in the basis functions as we like. For any choice, finely resolved or coarsely resolved basis functions, our interpretation of the expansion of the distribution function into slowing-down basis functions as slowing-down physics regularization holds.
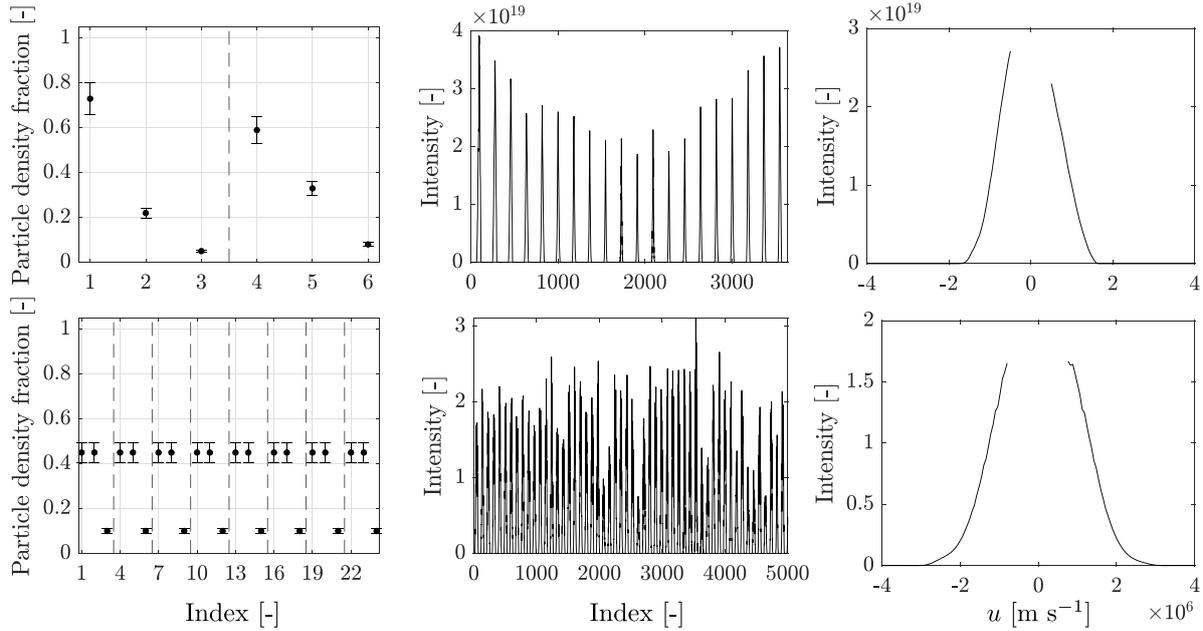
Figure 6. Essential aspects of the dataset for TCV (top row) and W7-X (bottom row). The first column shows the values of the densities of each beam component with 10% variation in each coordinate. The 'Index' label refers to the energy beam components in each neutral beam injector. The second column shows example data vectors s with all projected spectra ordered sequentially in a single vector. The 'Index' label here refers to each measurement bin in the projected spectra. The third column shows a single spectrum illustrating the shape of the spectral peaks as a function of the projected velocity u cut off at $\pm 0.5 \times 10^6 \ \text{m s}^{-1}$.

6. Generation of synthetic data based on the ground truth

The study of slowing-down physics regularization using Tikhonov regularization is performed on synthetic measurement data based on ASCOT5 and BEAMS3D simulations for TCV and W7-X. In both simulations, particles slow down due to Coulomb collisions until they reach twice the thermal energy. For TCV, phase space was discretized using a grid of size $(50, 150, 40, 40)$ for $(R, Z, v_\parallel, v_\perp)$ with corresponding ranges $([0.62, 1.14] \text{m}, [-0.75, 0.75] \text{m}, [-1.8 \times 10^6, 1.8 \times 10^6] \text{m s}^{-1}, [0, 1.8 \times 10^6] \text{m s}^{-1})$. For W7-X, phase space was discretized using a grid of size $(41, 34, 51, 32, 16)$ for $(R, \theta, Z, v_\parallel, v_\perp)$ with corresponding ranges $([4.5, 6.5] \text{m}, [0, 2\pi], [-1, 1] \text{m}, [-4 \times 10^6, 4 \times 10^6] \text{m s}^{-1}, [0, 4 \times 10^6] \text{m s}^{-1})$. The synthetic measurement data is generated by computing $Wf = s$ for known f which we refer to as the ground truth. The fast-ion phase-space distribution functions f are generated by specifying the values in the coefficient vector c and performing the multiplication $f = \Psi c$. Due to the generation mechanisms of the deuterium ions in the neutral beams, the density fractions for the distribution functions of deuterium monomers, dimers, and trimers are 0.73:0.22:0.05 and 0.59:0.33:0.08 for NB1 and NB2 at TCV at the nominal energies 25 keV and 47 keV and 0.45:0.45:0.10 for the NBIs at W7-X at the nominal energy 55 keV. The values in c are generated with a 10% variation of these values for each energy beam coefficient. This value for the variation was chosen since it is larger than the expected experimental error of the injected density fractions of the NBIs and typical for experimental error. The projection data comprise spectra from many lines of sight, and

these are stacked in a single vector s. The values of the sought coefficients and example spectra are illustrated in figure 6.

If the same model is used to compute the synthetic spectra and the inference of the distribution function, the inference is unrealistically easy. This is sometimes called an 'inverse crime' [46]. To avoid committing an inverse crime when solving the inverse problem $W\Psi c = s$, the dimensions of the weight function matrix used to solve the inverse problem must be different from the dimensions of the weight function matrix used to generate the data. For TCV, the grid size used to generate the data was [40, 40] and the inversion grid size [37, 37]. For W7-X, the corresponding grid sizes were [32, 16] and [33, 17]. Furthermore, noise is added to each measurement to simulate actual measurements, such that the signal-to-noise ratio is up to 10%.

For W7-X, we investigate two scenarios: one with 250 lines of sight and one with 680 lines of sight, with viewing angles calculated for FIDA views located in available ports. Each line of sight passes through NBIs Q7 and Q8, so a spectrum measured by one spectrometer is the sum of the signals from FIDA emission from its intersections with Q7 and Q8. Thus, the signal $s_i = W_7 f_7 + W_8 f_8$ for the weight functions W_7 and W_8 associated with NBIs Q7 and Q8 for the specific FIDA view i.

7. Simulation results

The difficulty of determining the correct coefficient vector c increases with the number of active beams. Therefore, we show the reconstructions with all beams active: two at TCV
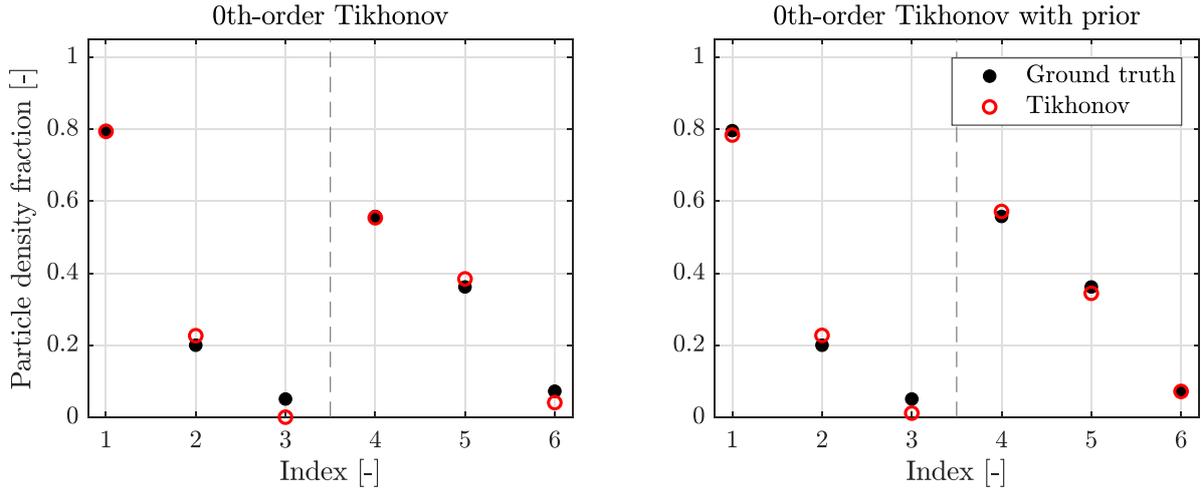
Figure 7. Reconstructions from synthetic measurements from TCV. The black dots indicate the actual densities (ground truth) for each beam energy component, and the red circles correspond to the density computed using 0th-order Tikhonov with and without priors.

and eight at W7-X—and noting that reconstructions for fewer active beams are as accurate or better.

7.1. TCV with 20 lines of sight and W7-X with 250 lines of sight

The 4D and 5D phase-space distribution functions are determined by solving the equation

$$c^* = \arg\min_{c} \left\{ \|W\Psi c - s\|_2^2 + \sum_k \lambda_k^2 \|L_k c\|_2^2 \right\} \text{ subject to } \Psi c \geqslant 0 \tag{16}$$

and subsequently computing $f^* = \Psi c^*$. With this notation, $k \in \{0, 1\}$ corresponding to 0th-order and 1st-order Tikhonov regularization. For all techniques, the optimal values of λ_0 and λ_1 are determined by choosing the solution to equation (16) with the lowest mean 2-norm deviation

$$\Delta_2 := \frac{1}{N} \|c^* - c^{\text{exact}}\|, \tag{17}$$

where c^{exact} is the ground truth and N the number of coefficients; $N = 6$ for TCV and $N = 24$ for W7-X.

The case of $k = 0$ called '0th-order Tikhonov regularization' corresponds to solving

$$c^* = \arg\min_{c} \left\{ \|W\Psi c - s\|_2^2 + \lambda_0^2 \|L_0 c\|_2^2 \right\} \quad \text{subject to} \quad \Psi c \geqslant 0 \tag{18}$$

with λ_0 a scalar, and $L_0 = I$. The reconstructions for TCV and W7-X using 0th-order Tikhonov regularization are illustrated in figures 7 and 8. In a perfect reconstruction, the red circles (reconstructions) enclose the black dots (ground truth). Note that the reconstruction is systematically biased: penalizing the 2-norm of the coefficient vector c tends to decrease the largest values, here the half-energy beam component values of 0.45, and tends to increase the lowest values. This is a deficiency

that the 0th-order Tikhonov regularization always has. We can observe this tendency in our inversions, though the regularization parameter can be so low that the data dictates otherwise, as is the case for the one-third energy components. However, decreasing the regularization parameter λ_0 to allow more variation in the coefficient values decreases the accuracy of the reconstruction further. To avoid this tendency of the 0th-order Tikhonov regularization, we use prior information or 1st-order Tikhonov regularization.

We may use the prior information that the expected values of the nominal beam coefficients are particle density fractions obtained by other means, e.g. by measurement of the beam emission or physics of the acceleration phase of the atoms in the neutral beam injectors. In our numerical test, we can use the ground truth. Note that this is not the ground truth of a given test case since 10% noise is added to each coefficient before generating the signal. Thus, this prior has the tendency to bias the solution towards this prior information. We view this as an advantage over biasing larger values downwards.

Denote by c_0 the vector with the values of the nominal beam coefficients for each beam component. Then, the 4D and 5D phase-space distribution functions are determined by solving

$$c^* = \arg\min_{c} \left\{ \|W\Psi c - s\|_2^2 + \lambda_0^2 \|L_0 (c - c_0)\|_2^2 \right\} \text{ subject to } \Psi c \geqslant 0. \tag{19}$$

We call this technique '0th-order Tikhonov regularization with prior'; see figures 7 and 8 for the reconstructions for TCV and W7-X using this technique. The 0th-order Tikhonov regularization with prior reconstructions is better than the one without prior for both TCV and W7-X. The regularization strengths used for 0th-order Tikhonov regularization with and without prior information are different due to the numerical differences of c and $c - c_0$.

An alternative to the 0th-order Tikhonov regularization is 1st-order Tikhonov regularization which, in general, penalizes differences between neighboring pixels. Here, our prior information is that the NBI's installed at W7-X are constructed and operated in the same way and, therefore, have the same species mix, i.e. the full-energy coefficients are likely the same for all NBIs, as are the half-energy coefficients, and the third energy coefficients. Since the two beams at TCV have different particle density fractions for the full, half, and third energy components, we should not penalize differences in the corresponding particle fractions for the current beam setup at TCV.

Thus, a relevant prior for the 24 coefficients at W7-X is

$$a_{3n+1} \approx a_1, \qquad (20)$$

$$a_{3n+2} \approx a_2, \qquad (21)$$

$$a_{3n+3} \approx a_3, \qquad (22)$$

for $n = 1, 2, \ldots, 7$. This prior belief can be written as the penalty matrix

$$\boldsymbol{L}_1 = \begin{pmatrix} 1 & 0 & 0 & -1 & 0 & \cdots & 0 \\ 0 & 1 & 0 & 0 & -1 & \cdots & 0 \\ & & \ddots & & & \ddots & \\ 0 & 0 & \cdots & 1 & 0 & 0 & -1 \end{pmatrix}. \qquad (23)$$

Since this matrix penalizes differences between similar energy components among different beams, we call this '1st-order Tikhonov regularization.' Thus, for $k = 1$, the equation to be solved is

$$\boldsymbol{c}^* = \min_{\boldsymbol{c}} \left\{ \|\boldsymbol{W}\boldsymbol{\Psi}\boldsymbol{c} - \boldsymbol{s}\|_2^2 + \lambda_1^2 \|\boldsymbol{L}_1\boldsymbol{c}\|_2^2 \right\} \quad \text{subject to} \quad \boldsymbol{\Psi}\boldsymbol{c} \geqslant 0 \qquad (24)$$

with λ_1 a scalar.

The 1st-order Tikhonov regularization solution is much better than that found by 0th-order Tikhonov regularization. The third energy components are determined almost perfectly, and the full- and half-energy components from the solution are around the correct values. However, the values of the solutions for the full- and half-energy beam components are biased in the direction of the majority of the beam components. For example, if more than four of the true full-energy beam component coefficients are larger than 0.45 due to noise, the 1st-order Tikhonov regularized solution for the full-energy beam components will be greater than 0.45 for all beams. The situation is the same for the half-energy beam component. However, this behavior could be an advantage since the eight NBIs are assumed to be constructed identically and, therefore, any systematic effects will be found by 1st-order Tikhonov regularization. See a reconstruction example for W7-X in figure 8.

Further, a 0th-order Tikhonov prior can be imposed on the 1st-order Tikhonov regularization. This corresponds to solving

$$\boldsymbol{c}^* = \min_{\boldsymbol{c}} \left\{ \|\boldsymbol{W}\boldsymbol{\Psi}\boldsymbol{c} - \boldsymbol{s}\|_2^2 + \lambda_0^2 \|\boldsymbol{L}_0 (\boldsymbol{c} - \boldsymbol{c}_0)\|_2^2 + \lambda_1^2 \|\boldsymbol{L}_1\boldsymbol{c}\| \right\}$$
$$\text{subject to} \quad \boldsymbol{\Psi}\boldsymbol{c} \geqslant 0. \qquad (25)$$

The equation is implemented in the following form

$$\boldsymbol{c}^* = \arg\min_{\boldsymbol{c}} \left\| \begin{pmatrix} \boldsymbol{W}\boldsymbol{\Psi} \\ \lambda_0\boldsymbol{I} \\ \lambda_1\boldsymbol{L} \end{pmatrix} \boldsymbol{c} - \begin{pmatrix} \boldsymbol{s} \\ \lambda_0\boldsymbol{c}_0 \\ 0 \end{pmatrix} \right\|_2. \qquad (26)$$

See a reconstruction example for W7-X in figure 8. The prior improves the 1st-order Tikhonov regularized solution by mitigating the bias in the solution: the amplitudes of the full- and half-energy components are closer to the actual values, and the third-energy components are determined perfectly.

The spatial and velocity distribution functions corresponding to the reconstructed coefficient vectors are illustrated in figure 9 for 0th-order Tikhonov regularization. Observe that the reconstructed distributions are almost identical to the true distributions, indicating the applicability of the technique to determine coefficient vectors corresponding to the underlying true distributions.

7.2. W7-X with 680 lines of sight

Physical constraints such as port access and space for spectrometers within ports restrict the available measurement volumes and the corresponding viewing angles. At W7-X, 17 ports located in the first- and second half-modules of the second module are here considered suitable for the installation of additional FIDA views. Thus, we investigate the maximal reconstruction quality using all 17 ports with full beam coverage, i.e. the FIDA views in each port can span the full length of the Q7 and Q8 NBIs. Each port is chosen to have 40 lines of sight. This corresponds to $17 \times 40 = 680$ spectra with a resolution of 84 measurement bins for a total of 57 120 measurement points, a 270% increase in the amount of data available for reconstructions. We refer to figure 3 for the viewing angles of the 17 ports.

Tikhonov-regularized reconstructions from the data described above are illustrated in figure 10. Observe the significant improvement in the 0th-order regularized solution compared to that in figure 8. Of all the reconstructions shown in this paper, the 0th- and 1st-order Tikhonov reconstructions here produce the best results, as the values of the coefficients in the reconstructions are the closest to the ground truth using no prior information.
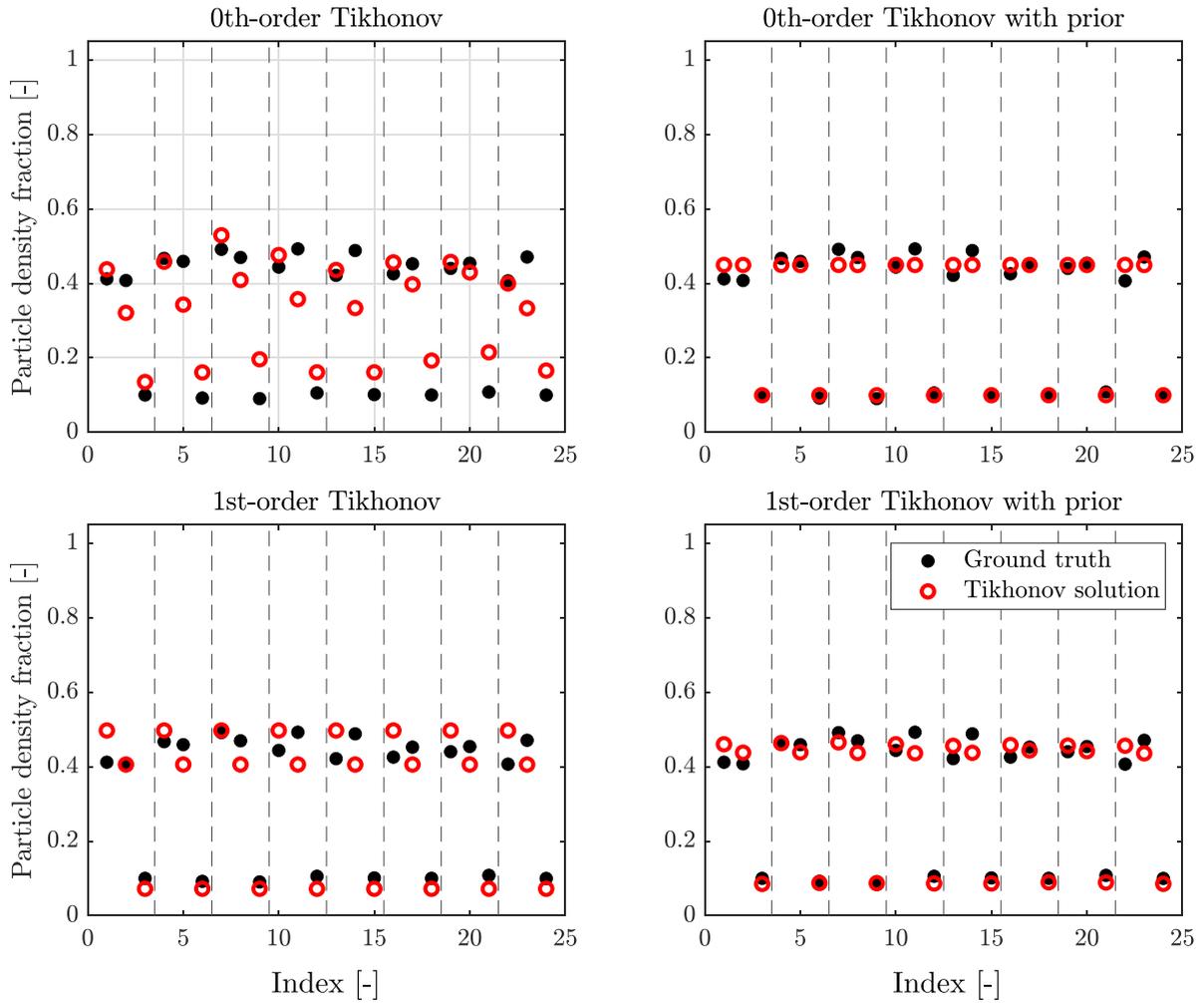
Figure 8. Reconstructions from synthetic measurements from W7-X. The black dots indicate the actual particle density fractions (ground truth) for each beam energy component, and the red circles correspond to the particle density fractions computed using 0th-order Tikhonov with and without priors (top row) and 1st-order Tikhonov with and without priors (bottom row).
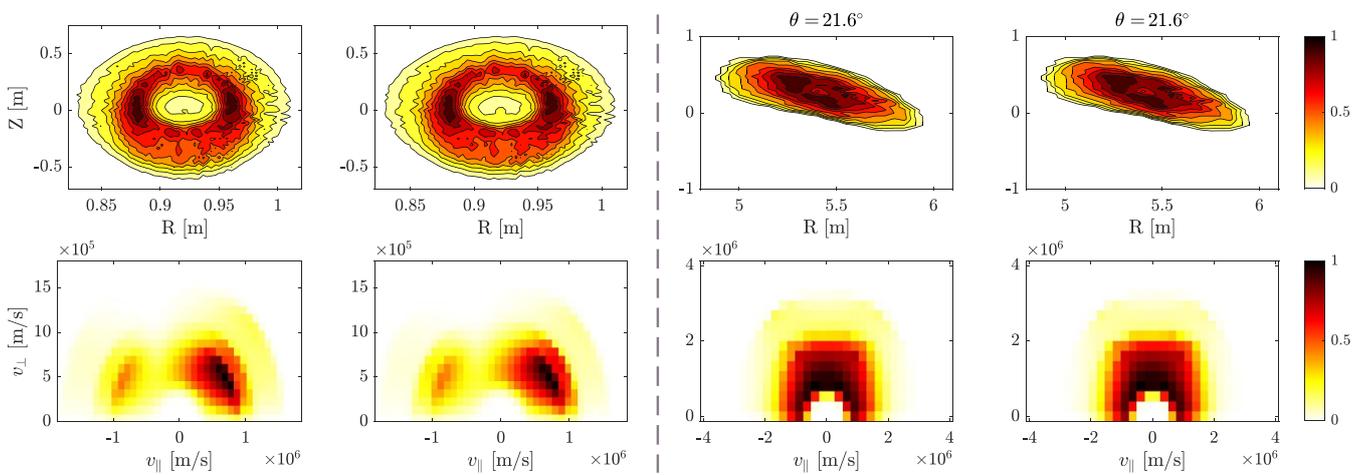
Figure 9. The first row contains spatial distributions for TCV (to the left of the dashed line) and W7-X (to the right of the dashed line), and the second row contains velocity distributions. The first and third columns show the actual distribution functions, and the second and fourth columns show the reconstructed solutions from Tikhonov regularization.
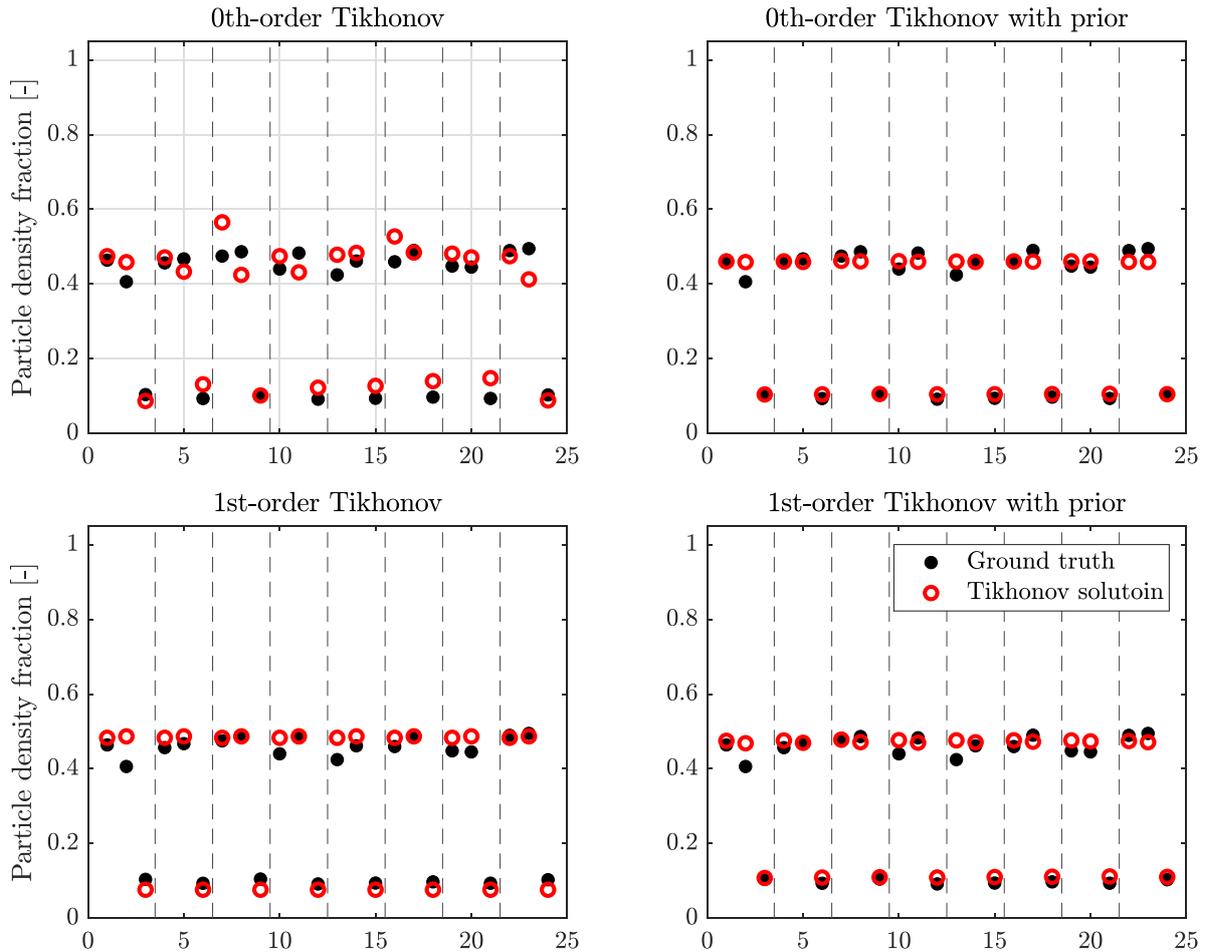
Figure 10. Reconstructions for a diagnostic setup at W7-X with 680 lines of sight distributed across 40 lines of sight in all 17 available ports in the first and second half-module of the second module.

8. Conclusion and Outlook

Reconstructing 4D and 5D fast-ion phase-space distribution functions at TCV and W7-X requires an approach beyond traditional Tikhonov regularization used for velocity-space tomography. The slowing-down physics regularized solution f^* lies in the vector space spanned by slowing-down distributions $\psi_1, \psi_2, \ldots, \psi_{\mathrm{sd}}$ such that $f^* = \sum_j c_j \psi_j$. The slowing-down distribution functions are calculated using ASCOT5 for TCV and BEAMS3D for W7-X. The slowing-down distribution functions ψ_j were calculated for the full, half, and one-third beam energy components for two neutral beams at TCV and eight neutral beams at W7-X.

In slowing-down physics regularization, the sought quantity is the column vector c containing the slowing-down distribution coefficients c_j. This column vector was obtained using Tikhonov regularization. We showed that for any number of grid points n and any number of slowing-down distribution functions N_{sd}, the expansion in slowing-down basis functions is equivalent to regularizing after slowing-down physics, i.e. using the regularizer $\mathbf{\Psi}^\dagger$ on f in Tikhonov regularization.

Slowing-down physics regularization can be successfully applied to synthetic measurements s to obtain the column vector c very close to the known ground truth. As a consequence, the reconstructed fast-ion phase-space distribution functions $f = \mathbf{\Psi}c$ are very similar to the ground truths. The best reconstructions are obtained with a larger amount of data. Therefore, we suggest installing as many views as possible in the available ports.

The next step is to increase the number of simulated slowing-down distribution functions along the neutral beam paths. Adding more slowing-down distribution functions corresponds to adding additional basis vectors to $\mathbf{\Psi}$, hence increasing the available fast-ion phase-space distribution functions that can be reconstructed. A very large numbers of lines of sight are expected to be crucial for this approach adding further support to the suggestion of installing as many views as possible.

Acknowledgments

ORCID iDs

B.S. Schmidt ⬤ https://orcid.org/0000-0001-5302-9489
M. Salewski ⬤ https://orcid.org/0000-0002-3699-679X
D. Moseev ⬤ https://orcid.org/0000-0001-7955-8565
P.C. Hansen ⬤ https://orcid.org/0000-0002-7333-7216
J. Eriksson ⬤ https://orcid.org/0000-0002-0892-3358
H. Järleblad ⬤ https://orcid.org/0000-0003-1126-686X
D. Kulla ⬤ https://orcid.org/0000-0003-1621-7338
S. Lazerson ⬤ https://orcid.org/0000-0001-8002-0121
M. Nocente ⬤ https://orcid.org/0000-0003-0170-5275
P. Poloskei ⬤ https://orcid.org/0000-0001-7781-5599
A. Snicker ⬤ https://orcid.org/0000-0001-9604-9666
L. Stagner ⬤ https://orcid.org/0000-0001-5516-3729
S. Äkäslompolo ⬤ https://orcid.org/0000-0002-9554-5147

References

[1] Moseev D. and Salewski M. 2019 *Phys. Plasmas* **26** 020901
[2] Budny R.V. *et al* 1995 *Nucl. Fusion* **35** 1497
[3] Pankin A., McCune D., Andre R., Bateman G. and Kritz A. 2004 *Comput. Phys. Commun.* **159** 157–84
[4] Grierson B.A. *et al* 2018 *Fusion Sci. Technol.* **74** 101
[5] Hirvijoki E., Asunta O., Koskela T., Kurki-Suonio T., Miettunen J., Sipilä S., Snicker A. and Äkäslompolo S. 2014 *Comput. Phys. Commun.* **185** 1310–21
[6] Lazerson S. *et al* 2020 *Nucl. Fusion* **60** 076020
[7] Mencke J.E., Moseev D., Salewski M., Larsen M.R., Schmidt B.S., Järleblad H., Lazerson S., Poloskei P.Z. and Ford O. 2022 *Rev. Sci. Instrum.* **93** 123503
[8] Kazakov Y.O. *et al* 2020 *Nucl. Fusion* **60** 112013
[9] Nocente M. *et al* 2020 *Nucl. Fusion* **60** 124006
[10] Nocente M. *et al* 2020 *Plasma Phys. Control. Fusion* **62** 014015
[11] Moseev D., Salewski M., Garcia-Muñoz M., Geiger B. and Nocente M. 2018 *Rev. Mod. Plasma Phys.* **2** 7
[12] Salewski M. *et al* 2014 *Nucl. Fusion* **54** 023005
[13] Weiland M., Geiger B., Jacobsen A.S., Reich M., Salewski M. and Odstrčil T. 2016 *Plasma Phys. Control. Fusion* **58** 025012
[14] Salewski M. *et al* 2016 *Nucl. Fusion* **56** 106024
[15] Weiland M., Bilato R., Geiger B., Schneider P.A., Tardini G., Garcia-Muñoz M., Ryter F., Salewski M. and Zohm H. 2017 *Nucl. Fusion* **57** 116058
[16] Madsen B., Salewski M., Huang J., Jacobsen A.S., Jones O. and McClements K.G. 2018 *Rev. Sci. Instrum.* **89** 10D125
[17] Madsen B. *et al* 2020 *Plasma Phys. Control. Fusion* **62** 115019
[18] Madsen B., Salewski M., Heidbrink W.W., Stagner L., Podestà M., Lin D., Garcia A.V., Hansen P.C. and Huang J. 2020 *Nucl. Fusion* **60** 066024
[19] Su J. *et al* 2021 *Plasma Sci. Technol.* **23** 095103
[20] Jacobsen A.S. *et al* 2016 *Plasma Phys. Control. Fusion* **58** 045016
[21] Jacobsen A.S., Salewski M., Geiger B., Korsholm S.B., Leipold F., Nielsen S.K., Rasmussen J., Stejner M. and Weiland M. 2016 *Plasma Phys. Control. Fusion* **58** 042002
[22] Salewski M. *et al* 2017 *Nucl. Fusion* **57** 056001
[23] Salewski M. *et al* 2018 *Fusion Sci. Technol.* **74** 23–36
[24] Galdon-Quiroga J. *et al* 2018 *Phys. Rev. Lett.* **121** 025002
[25] Galdon-Quiroga J. *et al* 2019 *Nucl. Fusion* **59** 066016
[26] Salewski M. *et al* 2019 *J. Instrum.* **14** C05019
[27] Schmidt B., Salewski M., Reman B., Dendy R.O., Moseev D., Ochoukov R., Fasoli A., Baquero-Ruiz M. and Järleblad H. 2021 *Rev. Sci. Instrum.* **92** 053528
[28] Stagner L., Heidbrink W.W., Salewski M., Jacobsen A.S. and Geiger B. (the DIII-D and ASDEX Upgrade Teams) 2022 *Nucl. Fusion* **62** 026033
[29] McNeely P. *et al* 2020 *Fusion Eng. Design* **161** 111997
[30] Lazerson S.A. *et al* 2021 *Nucl. Fusion* **61** 096008
[31] Heidbrink W.W., Luo Y., Burrell K.H., Harvey R.W., Pinsker R.I. and Ruskov E. 2007 *Plasma Phys. Control. Fusion* **49** 1457
[32] Heidbrink W.W. 2010 *Rev. Sci. Instrum.* **81** 10D727
[33] Salewski M. *et al* 2011 *Nucl. Fusion* **51** 083014
[34] Salewski M. *et al* 2014 *Plasma Phys. Control. Fusion* **56** 105005
[35] Jacobsen A.S., Salewski M., Eriksson J., Ericsson G., Korsholm S.B., Leipold F., Nielsen S.K., Rasmussen J. and Stejner M. 2015 *Nucl. Fusion* **55** 053013
[36] Jacobsen A.S., Binda F., Cazzaniga C., Eriksson J., Hjalmarsson A., Nocente M., Salewski M. and Tardini G. 2017 *Rev. Sci. Instrum.* **88** 073506
[37] Järleblad H., Stagner L., Salewski M., Eriksson J., Benjamin S., Madsen B., Nocente M., Rasmussen J. and Schmidt B.S. 2021 *Rev. Sci. Instrum.* **92** 043526
[38] Järleblad H., Stagner L., Salewski M., Eriksson J., Nocente M., Rasmussen J., Štancar Ž., Kazakov Y.O., Simmendefeldt B. and Contributors J. 2022 *Nucl. Fusion* **62** 112005
[39] Salewski M. *et al* 2015 *Nucl. Fusion* **55** 093029
[40] Salewski M. *et al* 2016 *Nucl. Fusion* **56** 046009
[41] Galdon-Quiroga J. *et al* 2018 *Plasma Phys. Control. Fusion* **60** 105005
[42] Heidbrink W.W., Garcia A., Boeglin W. and Salewski M. 2021 *Plasma Phys. Control. Fusion* **63** 055008
[43] Salewski M. *et al* 2012 *Nucl. Fusion* **52** 103008
[44] Salewski M. *et al* 2013 *Nucl. Fusion* **53** 063019
[45] Salewski M. *et al* 2018 *Nucl. Fusion* **58** 096019
[46] Hansen P.C. 2010 *Discrete Inverse Problems: Insight and Algorithms* (Philadelphia: SIAM)
[47] Pedersen T.S. *et al* 2020 *Nucl. Fusion* **62** 042022